Journal of Energy Storage 59 (2023) 106370

Contents lists available at ScienceDirect

Journal of Energy Storage

journal homepage: www.elsevier.com/locate/est

Research papers

Self-assembly CuO surface decorated with $NiAl_2O_4$ for high-temperature thermochemical energy storage: Excellent performance and strong interaction mechanism

Jiali Deng [a,b], Changdong Gu [c], Haoran Xu [a,b], Gang Xiao [a,b,*]

[a] State Key Laboratory of Clean Energy Utilization, College of Energy Engineering, Zhejiang University, Hangzhou, Zhejiang 310027, China
[b] Key Laboratory of Clean Energy and Carbon Neutrality of Zhejiang, Jiaxing Institute of Zhejiang University, 966 Xiuyuan Road, Jiaxing 314031, China
[c] State Key Laboratory of Silicon Materials, College of Materials Science and Engineering, Zhejiang University, Hangzhou, Zhejiang 310027, China

ARTICLE INFO

Keywords:
Self-assembly
Solar energy
Thermochemical energy storage
Cycling stability
Sinter resistance
Modification mechanism

ABSTRACT

High-temperature thermochemical energy storage materials with high energy density is the key technical support for the third generation concentrated solar power plants equipped with advanced energy storage system. CuO/Cu_2O redox couple is one of the most promising systems due to its low cost and high energy density, but its application is limited by poor reaction performance. Herein, the self-assembly CuO surface decorated with 15 wt % $NiAl_2O_4$ is prepared with excellent redox reversibility and ultralong lifespan. Its reaction rate is increased by 4.2 times with re-oxidation degree increasing from 46 % to 99.9 %. The thermochemical energy density of storage and release reach −772.726 kJ/kg and 764.655 kJ/kg, respectively. After 1000 cycles, the degree of reduction and oxidation reaction can keep 99.9 % and 98 %. The material characterization shows that $NiAl_2O_4$ are uniformly and firmly loaded on the surface of CuO/Cu_2O, which significantly increases the sintering temperature and improves the reaction performance. DFT studies further confirm that $NiAl_2O_4$ has a high binding energy with CuO/Cu_2O and can increase the formation energy of copper vacancy. The study reveals the anti-sintering modification mechanism of CuO/Cu_2O by introducing $NiAl_2O_4$, which provides a solution toward sintering resistance of high-temperature thermochemical energy storage materials.

1. Introduction

The third generation concentrated solar power (CSP) plants require lower cost and higher efficiency technology, and high temperature can boost the efficiency of thermodynamic cycles [1]. Because thermochemical energy storage (TCES) technology has higher energy storage density and feasibility than sensible heat storage (SHS) at high temperature, it emerges as an attractive scheme for the design of the next generation of power plants [2]. The metal oxides redox system demonstrates many advantages of simpler system and better compatibility with CSP plants than other TCES systems (e.g. carbonate and hydroxide systems) [3–7], which is the most potential candidate for thermochemical energy storage based on solid-gas reversible reactions [8]. Co_3O_4/CoO, Mn_2O_3/Mn_3O_4 and CuO/Cu_2O are considered suitable for high temperature thermochemical energy storage materials [8–12]. Co_3O_4/CoO redox couple has excellent reversibility [13–17], but it presents the distinct drawbacks of high costs and carcinogenicity [2,8,9]. The most crucial problem of Mn_2O_3/Mn_3O_4 system is the slow oxidation kinetics, but Fe-doping can remarkably improve the reaction characteristics [2,18–22]. However, the energy storage density of this system is much lower than other redox couples [9]. CuO/Cu_2O couple has the advantages of wide availability, high energy density, and low hysteresis temperature gaps guaranteeing high exergy efficiencies [2]. Nevertheless, the melting point of Cu_2O is too close to the reduction temperature and this may result in severe sintering problem, resulting in incomplete oxidation of Cu_2O [7,8,10]. After multiple cycles, the particles show obvious shrinkage and densification induced a short cycle life [23,24]. Limit its large-scale multi-scenario application as thermochemical energy storage materials.

Alonso et al. [7] found that oxygen was released at about 500 °C for CuO/Cu_2O in argon while this value increased to 800 °C in air. And stronger coalescence of the particles was observed in air than in argon,

* Corresponding author at: State Key Laboratory of Clean Energy Utilization, College of Energy Engineering, Zhejiang University, Hangzhou, Zhejiang 310027, China.
E-mail address: xiaogangtianmen@zju.edu.cn (G. Xiao).

https://doi.org/10.1016/j.est.2022.106370
Received 27 July 2022; Received in revised form 10 November 2022; Accepted 8 December 2022
Available online 28 December 2022
2352-152X/

what may handicap the redox reaction. Setoodeh et al. [25] re-evaluated the effect of pressure for oxidation of Cu_2O to CuO through thermogravimetric analyses, and isothermally ran between 800 °C and 930 °C at different oxygen partial pressures (0.1, 0.2, 0.5, and 1.0 bar). This result reflected low oxygen partial pressures would go along with low equilibrium temperatures. Therefore, changing the atmosphere can benefit to promote the oxidation by alleviating sintering. But this approach can make the operation of the CSP system complicated. Steinfeld et al. [26] prepared porous CuO-based granules with yttria-stabilized zirconia (YSZ) as sintering inhibitor. They found CuO-YSZ granules exhibited stable cyclability over 100 consecutive cycles performed by TG in air between 950 °C and 1050 °C. However, YSZ is expensive and not suitable for extensive applications. Qasim et al. [27] investigated the feasibility of using $MgAl_2O_4$-stabilized oxygen carrier containing 70–90 wt% CuO in CLOU process. The results showed that the surface of the oxygen carrier covered with nano-sized $MgAl_2O_4$ grains can stabilize the thermal sintering and agglomeration of CuO-based oxygen carrier at 950 °C. However, $MgAl_2O_4$ was not uniformly distributed on the oxygen carrier in its material structure, and the grains of $MgAl_2O_4$ were obviously agglomerated, resulting in a large decrease in O_2 yield of material with high CuO content (90 wt%) observed in only 25 cycles. In addition, oxygen carrier typically undergo reduction at lower temperatures (~ 900 °C) in a nitrogen atmosphere, while metal oxides react directly with air in CSP and require higher reduction temperatures (~ 1020 °C). TCES materials face more severe sintering problems than oxygen carrier, so the rational design of the material is demanding. In previous work, we reported that the formation of $CuAl_2O_4$ after Al-doping could help to avoid the sintering problem, which increased the formation energy of copper vacancy in copper oxides [28]. The initial oxidation ratio of Cu_2O reached 99.5 % and remained 81.1 % after 120 cycles. Whereas, $CuAl_2O_4/CuAlO_2$ also underwent redox phase transformation in the reaction process, but their reaction performance was not good, so that the performance decay was fast after only 120 cycles. Moreover, due to the loss of some CuO which reacted with Al_2O_3, the energy storage/release density of CuO/Cu_2O decreased. The structural design of their composites is somewhat inadequate, which may lead to the decrease of sintering resistance and reactivity after repeated utilization. To sum up, it is necessary to reasonably design TCES material structure with long lifetime considering both the sinter-resistance and cyclic redox activity. At the same time, a simplified synthesis strategy with high yield and good reproducibility needs to be developed.

In this study, we designed the material structure of self-assembled $NiAl_2O_4$ surface decorated CuO. The design of the composite structure can ensure the CuO/Cu_2O reaction performance and maximize the retarding effect of inhibitor on CuO/Cu_2O sintering. Additionally, the composite was successfully synthesized by a simple preparation method, which greatly improved the re-oxidation degree, reaction kinetics and cycling stability. The improvement mechanism of $NiAl_2O_4$ spinel sintering inhibitor on CuO/Cu_2O performance was expounded through material characterization. Moreover, we also described density functional theory (DFT) calculations that analyzed the strong interaction between the $NiAl_2O_4$ and CuO/Cu_2O and compared the formation energy of copper vacancy, to jointly reveal the anti-sintering mechanism of the modified material. This research can provide guidance for the synthesis and design of other sinter-resistant metal oxides.

2. Material and methods

2.1. Material preparation

The self-assembly CuO surface decorated with $NiAl_2O_4$ were prepared by combining the sol-gel method and the high-temperature solid-phase method, in which the spinel structure inhibitor was prepared by the sol-gel method, and then was decorated on the CuO surface by the high-temperature solid-phase method. 0.1 mol Ni $(NO_3)_2{\cdot}6H_2O$, 0.2 mol Al $(NO_3)_2{\cdot}9H_2O$ and 0.3 mol of citric acid were dissolved in an appropriate amount of deionized water, stirred at 70 °C for 3 h, and then 0.2 mol ethylene glycol was added at 90 °C and stirred for 2 h. Then the gel was dried at 200 °C for 3 h, calcined firstly at 450 °C for 4 h, and at 800 °C for 4 h. The $NiAl_2O_4$ spinel structure inhibitor could be obtained. The composites were synthesized by mixing CuO and prepared $NiAl_2O_4$ powders uniformly in a planetary ball mill for 30 min and calcining at 900 °C for 4 h. The doping mass fraction ratios of CuO and $NiAl_2O_4$ in the samples were 95 wt%: 5 wt%, 90 wt%: 10 wt%, 85 wt%: 15 wt%, 80 wt %: 20 wt%, labeled NA-5, NA-10, NA-15 and NA-20, respectively.

2.2. Material characterizations

All samples in this paper were tested in powder form. X-ray diffraction (XRD) patterns were recorded with a X-pert Powder diffractometer in the range of 2θ of 10° to 80° by using Cu Kα (λ = 1.5406 Å) radiation. The scan step size was 0.02° and 20 s counting time per angle. The generator voltage and tube current were 40 kV and 40 mA, respectively. The field emission scanning electron microscopic (FESEM) imaging and energy-dispersive X-ray spectroscopy (EDS) mapping were carried out by a SU-8010 microscope. The BET surface area of samples was determined by using nitrogen adsorption-desorption isotherms measured at 77 K on the ASAP2460 automatic specific surface and micropore size analyzer. Fourier Transform Infrared Spectroscopy (FTIR) was used to study the chemical binding nature of the synthesized products taking by a Thermo Scientific Nicolet iS20 spectrometer in the range 400–4000 cm^{-1}, and the samples were prepared by the KBr disk method. X-ray photoemission spectroscopy (XPS) was performed using a Thermo Scientific K-Alpha electron energy analyzer and a monochromatized Al Kα X-ray photon source (hv = 1486.6 eV).

2.3. Material performance testing

TGA/DSC3+ simultaneous thermal analyzer was used to test and analyze the redox reactivity of the powder samples. The test atmosphere was air, which was consistent with the real application scenario. Air acted as both a heat transfer fluid and a reaction medium. The test temperature range was 50 °C -1100 °C -700 °C at a heating/cooling rate of 20 K/min under a continuous air flow of 50 mL/min for ~10 mg samples. Reduction reaction (endothermic) occurred during heating, followed by oxidation (exothermic) occurs during cooling.

2.4. DFT computation details

Spin-polarized DFT calculations were carried out using plane wave basis sets for valence electrons and projector augmented wave (PAW) potentials for core electrons [29], as implemented in the Vienna Ab Initio Simulation Package (VASP) [30]. The generalized gradient approximation (GGA) with the Perdew-Burke-Ernzerhof (PBE) exchange-correlation functional was used [31]. The plane-wave basis sets with a kinetic energy cutoff of 500 eV were set. Considering the strong electron correlation effects of Cu and Ni, the calculations were performed with the DFT + U method [32]. According to previous reports, the parameters were taken as U = 7 eV for Cu [33] and 6.3 eV for Ni [34]. Monkhorst-Pack k-point meshes were used for the Brillouin zone integration as given in Table S1. Geometry optimization was employed using a convergence criterion of 1.0×10^{-4} eV for total energy and 0.02 eV/Å for maximum force on the atoms. The lattice constants evaluated by DFT calculations agree with experimental values with small deviations, as shown in Table S2. These results indicated that the DFT calculation was reliable for geometry optimization. CuO (111), Cu_2O (111) and $NiAl_2O_4$ (111) surface were used in this study because they were the most stable low index surfaces, mainly exposed to the environment [35,36]. The constructed slab model consisted of a 2 × 2 surface unit cell. In the surface slab calculations, the vacuum thickness was ~20 Å. The detailed structural parameters of slab models are listed

in Table S3.

3. Results and discussion

3.1. Characterization of As-prepared samples

Fig. 1 illustrates schematically the design idea and self-assembly preparation process of the composite. The phase composition and crystal structure of the as-prepared materials were obtained by X-ray diffraction analysis. The samples with different $NiAl_2O_4$ doping ratios are only composed of CuO (ICDD-PDF No. 48–1548, C2/c monoclinic space group) and $NiAl_2O_4$ (ICDD-PDF No. 73–0239, $Fd\bar{3}m$ cubic space group), and no diffraction peaks of impurities are indexed (Fig. S1). CuO and $NiAl_2O_4$ had sharp diffraction peaks, implying good crystallinity. FESEM images of different fresh samples are demonstrated in Figs. 2 and S2. The CuO particle size (~ 1 μm) without heat treatment was smaller and easy to agglomerate, while the grain growth of $NiAl_2O_4$ modified samples after high temperature treatment led to the increase of particle size (~ 4–5 μm). In addition, $NiAl_2O_4$ nanoparticles were uniformly distributed on the surface of CuO microparticles of NA-5, NA-10, NA-15 and NA-20. The load on the surface of the samples increased with the mass percentage of $NiAl_2O_4$. Moreover, there was good dispersion between the CuO particles, indicating that the self-assembly CuO surface decorated with $NiAl_2O_4$ were successfully synthesized.

3.2. Redox reaction performance

The redox performance of the as-prepared samples are presented in Fig. 3. The reduction of CuO could reach the theoretical weight loss (~ 10.02 %), but the weight gain of its oxidation process was only 4.6 % (Fig. 3a and c). Moreover, the re-oxidation rate was slower compared to the time required to complete the reduction, with only 46 % of the re-oxidation degree still requiring 13.2 min (Fig. 3b). The mass percentage of CuO decreased with the increase of $NiAl_2O_4$ doping. Since the substance in which redox occurred was CuO/Cu_2O, the reaction degree was reduced correspondingly. For each increase of 5 wt% $NiAl_2O_4$, the reaction degree decreased by about 0.55 %. The weight gain of NA-5, NA-10, NA-15 and NA-20 are 9.05 %, 8.77 %, 8.22 % and 7.63 %, respectively. Even the introduction of a small amount of $NiAl_2O_4$ could effectively improve oxidation performance. Except for NA-5 sample, the oxidation of other materials could be completed in 3.2–3.7 min. Overall, the CuO/Cu_2O surface decoration of $NiAl_2O_4$ has better reversibility and faster reaction rate.

3.3. Sintering mitigation

The sintering process of different materials at high temperatures is shown in Figs. 4 and S3. CuO was sintered at 1000 °C to form densified hard lumps (~15 μm), which began to melt as the temperature rose to 1040 °C (~23 μm) and completely melted at 1060 °C (~26 μm). CuO was only sintered before reduction (~1020 °C) but melted after completion of reduction (~1060 °C). However, CuO could be completely converted into Cu_2O, and Cu_2O was known to have poor thermal stability at high temperatures. Therefore, it is reasonable to speculate that the melting is caused by Cu_2O, and the coalescence and sintering of CuO in the early stage aggravate its melting. Nevertheless, no obvious sintering and melting phenomena were observed in the $NiAl_2O_4$ modified samples before ~1060 °C. In contrast, NA-5 may be due to less doping, resulting in some particles with surface incompletely decorated can still contact each other to sinter (~11 μm at 1060 °C) and further melt (~20 μm at 1100 °C) under harsh conditions of higher temperature, so its corresponding re-oxidation performance is slightly inferior to other three samples (Fig. 3). NA-15 and NA-20 only had smaller and less densified hard lumps (~5 μm and ~ 6 μm, respectively) caused by slight sintering within 1100 °C, which significantly increased the sintering temperature. Thus, the appropriate and effective $NiAl_2O_4$ surface decoration can greatly solve the agglomeration, sintering and melting problems of CuO/Cu_2O at high temperatures.

3.4. Thermochemical energy storage density and cycling life

The most important factor affecting the energy density and cycling performance of CuO/Cu_2O was serve sintering at high temperatures. Surprisingly, from the foregoing results, the NA-15 sample could greatly alleviate sintering while ensuring more redox. Fig. 5 manifests the energy density and cycle performance of NA-15. In the first cycle, the thermochemical energy storage density of NA-15 in the reduction stage reached −772.726 kJ/kg, and the energy release density during the oxidation was still 764.655 kJ/kg (Fig. 5a). However, the thermochemical energy release density of CuO in the first cycle was only 466.23 kJ/kg (Fig. S4). These results indicated that NA-15 had higher thermochemical energy storage and release density. The material underwent a complete reduction and oxidation reaction as a cycle. The cyclic reactivity of undoped CuO/Cu_2O is demonstrated in Fig. S5. After only 40 cycles, the re-oxidation degree attenuated to 28 %. As shown in Fig. 5b and c, NA-15 sample still has excellent redox activity after 1000 cycles. The reduction and re-oxidation degree kept 99.9 % and 98 %, respectively. It showed that the modification of the CuO/Cu_2O surface by 15 wt% $NiAl_2O_4$ greatly improves the cycle life of CuO/Cu_2O.

FESEM was used to analyze the influence of different cycles on the micromorphology of the samples, and to determine the grain changes after multiple cycles. The FESEM images of undoped CuO with different cycles are shown in Fig. S6. There was serious agglomeration and sintering between particles after only 10 cycles (~ 26 μm). With the progress of the cycle, the grain fusion and grain boundary blur, the sintered body was significantly densified after 40 cycles (~ 30 μm). However, the different cycles of NA-15 samples have excellent particle dispersion (Fig. 6). The particles were small after the first cycle (~ 4 μm), as shown in Fig. S7. From 1 to 200 cycles, the grain size increased (~ 4–10 μm) rapidly due to the aggregation and merge of small and large grains, which was driven by the difference in surface energy of different grain sizes (Ostwald ripening) [22]. The particle size of NA-15 tended to be constant after 200 cycles (~ 10 μm), indicating that surface-dispersed $NiAl_2O_4$ effectively inhibited coalescence between CuO particles. In addition, the particle size of NA-15 after 200–1000 cycles (~ 10 μm) was about 1/3 of that of undoped CuO after 10 cycles (~ 26 μm). The small $NiAl_2O_4$ grains were still uniformly and firmly loaded on the CuO surface even after 1000 cycles. It is speculated that

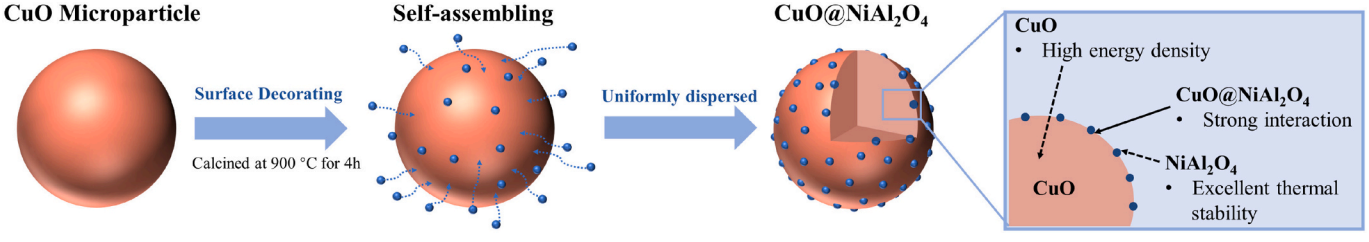

Fig. 1. Schematics of the self-assembly preparation process and morphologic characteristics of the CuO surface decorated with $NiAl_2O_4$.

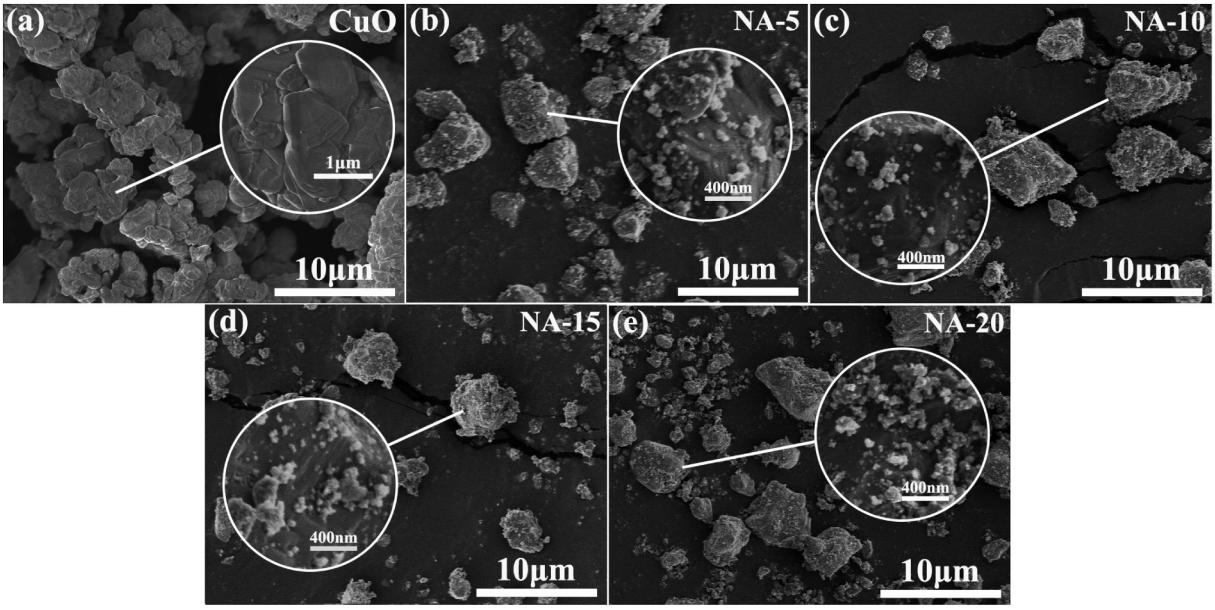

Fig. 2. FESEM images of fresh samples: (a) CuO, (b) NA-5, (c) NA-10, (d) NA-15, (e) NA-20.

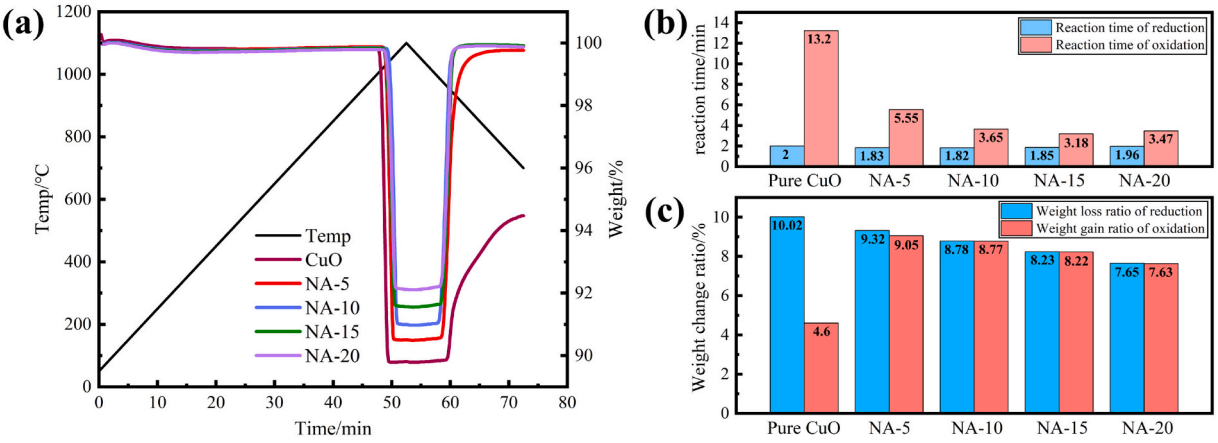

Fig. 3. Redox reaction performance of $NiAl_2O_4$ modified CuO/Cu_2O: (a) TG curves, (b) Reaction time, (c) Weight change ratio.

the $NiAl_2O_4$ inhibitor has strong interaction with metal oxides, thereby ensuring that the CuO/Cu_2O surface decorated by 15 wt% $NiAl_2O_4$ had excellent long-life redox reactivity.

The samples size change caused by particle sintering after different cycles were further confirmed by Brunauer-Emment-Teller (BET) analysis. The results are listed in Table 1. The BET surface area of CuO after first cycle was 1.0509 m^2/g, while decreased to 0.3087 m^2/g after 40 cycles. The specific surface area reduced dramatically by 3.4 times, indicating that there was serious coalescence and sintering between the particles. The BET surface area of NA-15 was 1.4964 m^2/g after the first cycle. The specific surface area of NA-15 was larger than that of CuO due to the smaller particle size of $NiAl_2O_4$ decorated on the surface of CuO and the inhibitor prevented the agglomeration of CuO. Due to the grain growth of NA-15, its specific surface area decreased to 0.8753 m^2/g after 200 cycles. However, the BET surface area after 1000 cycles kept 0.7650 m^2/g, which was close to the results of 200 cycles, elaborating that the grain size remained stable and there was no serious sintering. The specific surface area after 1000 cycles was still 2.48 times larger than that after 40 cycles of CuO. Therefore, the CuO material surface decorated with $NiAl_2O_4$ had excellent cycle stability and reaction activity.

3.5. *Physicochemical properties of NA-15 with excellent performance*

The physicochemical properties of NA-15 with excellent performance were deeply analyzed to explain the modification mechanism, and the characterization results are shown in Figs. 7 and 8. In order to clarify the phase structure evolution process of NA-15 in redox reaction, the samples at different stages were tested by XRD. As shown in Fig. 7a, CuO turned into Cu_2O after reduction reaction. The results of oxidized samples showed that no obvious Cu_2O diffraction peak appeared, and the phase was consistent with the fresh sample. It indicated that the whole reaction process had excellent reversibility and $NiAl_2O_4$ significantly improved the re-oxidation (Fig. 3). It could be obviously observed that there was more Cu_2O in the oxidized sample (Fig. 7b), so its re-oxidation degree was low. In addition, it is worth noting that the $NiAl_2O_4$ of spinel-type structure maintained a stable phase structure during the reaction, with the same diffraction peak intensity and good crystallinity. Therefore, it could be inferred that the inert inhibitor material had excellent chemical thermal stability in the operating temperature range. Moreover, $NiAl_2O_4$ didn't react with CuO/Cu_2O to form impurities, thereby avoiding damage to the reaction performance. The reaction equation of CuO surface decorated with $NiAl_2O_4$ can be deduced as follows:

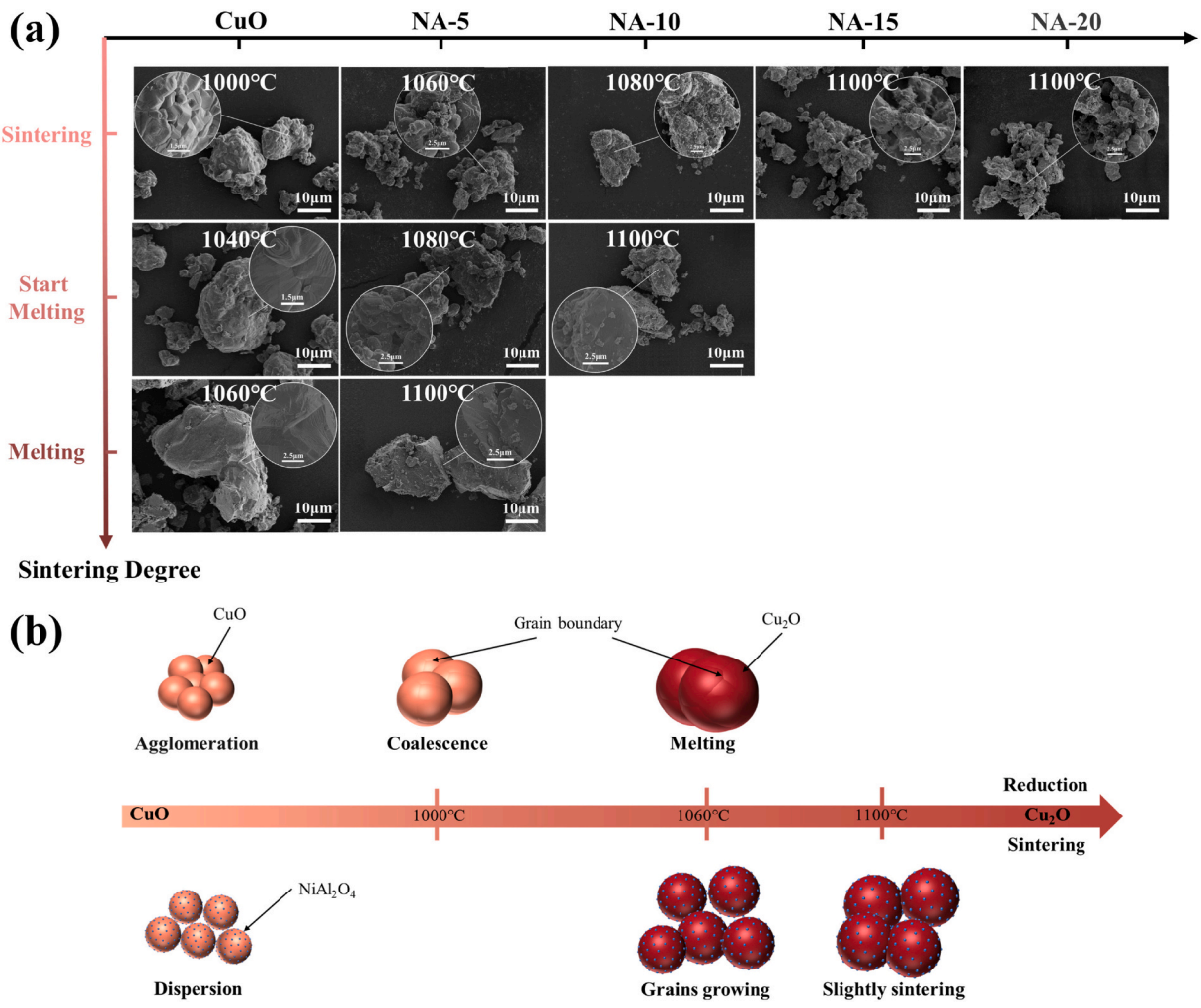

Fig. 4. Sintering process of different samples in operating temperature range. (a) FESEM images, (b) Schematic diagram.

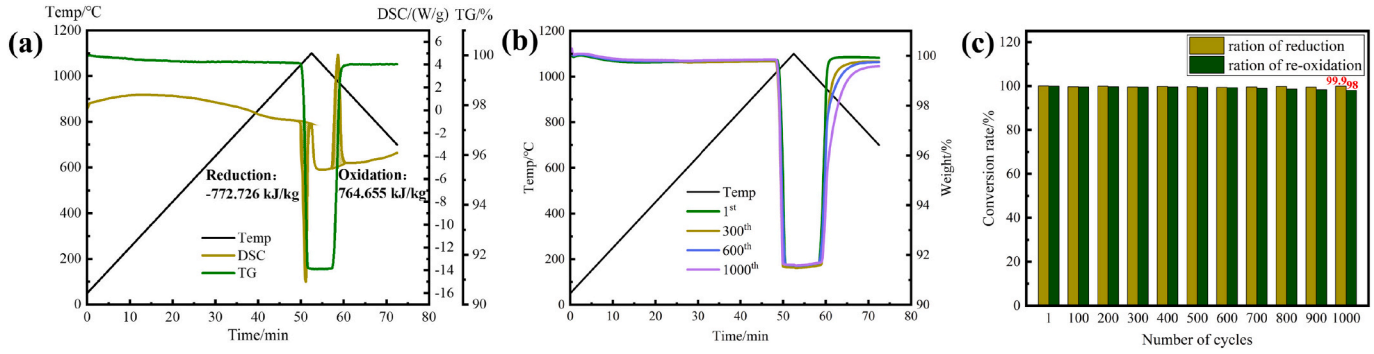

Fig. 5. Thermochemical energy storage density of NA-15 in the first cycle (a) TG-DSC curves. Long-life cycling performance over 1000 cycles (b) TG curves and (c) conversion rate.

$$4CuO + NiAl_2O_4 \rightleftharpoons 2Cu2O + O2 + NiAl_2O_4$$

NA-15 was tested and analyzed by SEM and EDS to further analyze the mechanism of $NiAl_2O_4$ on CuO/Cu_2O reaction performance improvement. There is an obvious adhesion between undoped Cu_2O particles to form dense and irregular larger particles (~ 23 μm) after reduction (Fig. S8), which was consistent with the melting phenomenon observed above (Fig. 4). This might be due to the migration-coalescence process of particles led to severe sintering. However, the particles remained densified (~ 24 μm) after 1st cycle. It is speculated that the reason why Cu_2O could not be completely oxidized to CuO lay in the densification of the material surface, which made it difficult for oxygen to diffuse into the inside of the particles. SEM image, EDS element mapping and EDS spectrum of NA-15 are shown in Figs. 8 and S9. Although CuO and Cu_2O underwent reversible phase transition, $NiAl_2O_4$ was firmly loaded on the surface of CuO/Cu_2O, suggesting a strong interaction between $NiAl_2O_4$ and CuO/Cu_2O. The size of the particles varied almost imperceptibly (~5 μm) and about 1/5 of undoped CuO. It indicated that the inhibitor with relatively small particle size decorated

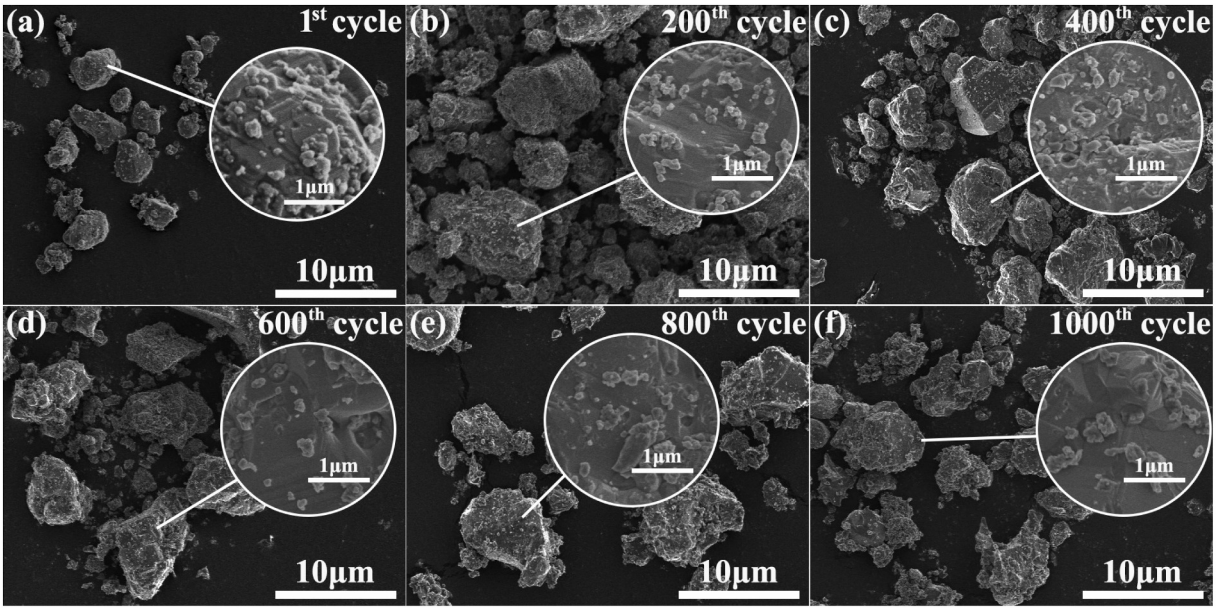

Fig. 6. FESEM images of NA-15 samples with different cycles: (a) 1st cycle, (b) 200th cycle, (c) 400th cycle, (d) 600th cycle, (e) 800th cycle, (f) 1000th cycle.

Table 1
Specific surface area of different samples at multiple cycles.

Metal oxides	Cycle number	BET (m^2/g)
CuO	1	1.0509
	20	0.7541
	40	0.3087
NA-15	1	1.4964
	200	0.8753
	1000	0.7650

on the metal oxides surface could ensure a large chemical reaction contact area and effectively prevent the agglomeration and sintering caused by CuO/Cu_2O particle contact. In addition, EDS element mappings clearly observed Cu, O, Ni and Al elements dispersed uniformly. $NiAl_2O_4$ was evenly distributed on the surface of CuO/Cu_2O particles, maximizing the confinement and preventing particles contact and merger, thus increasing the sintering temperature. In short, the uniform decoration of $NiAl_2O_4$ inhibitor can effectively improve the sintering resistance and the redox characteristics of the material.

The relationship between $NiAl_2O_4$ and CuO/Cu_2O was deeply analyzed by FTIR. The local enlargement spectra of 1000–400 cm^{-1} is shown in Fig. 7c and d. A broader spectrum of 4000–400 cm^{-1} is displayed in Fig. S10. The peaks of NA-15 at 498.54 cm^{-1}, 724.70 cm^{-1} and 720.09 cm^{-1} were attributed to the lattice vibration of Ni^{2+}-O^{2-} at octahedral sites and Al^{3+}-O^{2-} at tetrahedral sites [37]. There was a peak at 616.17 cm^{-1} associated with the stretching vibration of Cu^{+}-O^{2-} [38]. In addition, the peak of CuO after 1st cycle at 504.73 cm^{-1} corresponded to the Cu^{2+}-O^{2-} vibration in the monoclinic CuO [39]. It was worth mentioning that the peaks of Cu^{+}-O^{2-} and Cu^{2+}-O^{2-} in NA-15 appeared at 617.91 cm^{-1} and 522.26 cm^{-1}, respectively. Compared to undoped CuO, the positions of Cu—O peaks shifted to higher wavenumber after $NiAl_2O_4$ surface decoration. It indicated that there was charge transfer in NA-15 and strong interaction between CuO/Cu_2O and $NiAl_2O_4$. Thus, it is ensured that the inhibitor can firmly bind to CuO/Cu_2O, inhibiting the migration and sintering of CuO/Cu_2O.

The re-oxidation performance of the material decorated with $NiAl_2O_4$ was greatly improved, so the surface chemistry of the NA-15 sample after 1st cycle was analyzed by XPS. The Cu2p spectrum (Fig. 7e) consisted of Cu $2p_{3/2}$ and Cu $2p_{1/2}$, respectively. The binding energy were 933.2 eV in Cu $2p_{3/2}$, 953.1 eV in Cu $2p_{1/2}$, and the satellites represented Cu^{2+} species [40,41]. However, NA-15 samples had stronger Cu^{2+} peaks and satellites. CuO after 1st cycle had obvious and strong Cu^{+} peak at 931.4 eV and 951.3 eV [42], indicating that it was not completely oxidized, which was identical to the XRD pattern (Fig. 7b). Meanwhile, the Cu LM2 (Fig. 7f) spectrum also revealed that the characteristic peak of CuO sample at the binding energy of 569.5 eV corresponded to Cu^{+} [43]. Notably, NA-15 shifted to higher binding energy in the Cu 2p and Cu LM2 spectra, elucidating that the charge transfer in the sample led to changes in the electronic properties of Cu, which again confirmed the strong interaction between metal oxides and inhibitor. The two peaks of CuO at 528.8 eV and 530.3 eV in the O1s spectra (Fig. 7g) were the characteristics of lattice oxygen and adsorbed oxygen (including oxygen defects or a mixture of hydroxyl groups on CuO surface) [44]. Whereas, the peaks of NA-15 at 529.4 eV and 530.9 eV were also attributed to lattice oxygen and adsorbed oxygen, which was coincide with the previously reported $NiAl_2O_4$ [45]. NA-15 had more adsorbed oxygen than CuO, which was supposed to be ascribed to the surface decoration of $NiAl_2O_4$. More oxygen vacancies in $NiAl_2O_4$ can enhance the strong interaction between the active component and the inhibitor [46]. This is because the oxygen vacancy is electronegative, Cu metal cation entering the $NiAl_2O_4$ oxygen vacancy can form ionic bonds with it, which is conducive to strengthening the interaction.

3.6. Modification mechanism

The above experimental results had confirmed that alleviating CuO/Cu_2O sintering could effectively improve its reaction characteristics, so the sintering improvement mechanism of $NiAl_2O_4$ on CuO/Cu_2O was further revealed in combination with DFT calculation (Fig. 9). Based on the XRD analysis results (Fig. 7a), the interface models of the reduced and oxidized state are constructed (Fig. S11). The optimized slab models are shown in Fig. 9a and b. The binding energy ΔE_b of CuO-$NiAl_2O_4$ and Cu_2O-$NiAl_2O_4$ were − 26.861 eV and − 32.846 eV, respectively. They were greater than the values of CuO-CuO (−13.277 eV) and Cu_2O-Cu_2O (−12.299 eV). It manifested that compared with CuO-CuO/Cu_2O-Cu_2O self-coalescing, they were more inclined to bind with $NiAl_2O_4$ to make the whole system more stable, which could effectively solve the coalescence and sintering problem caused by surface contact and bonding of particles. Moreover, the bond lengths of Cu—O and Al—O of various models are exhibited in Table S4. The bonds at the interface of CuO/Cu_2O-$NiAl_2O_4$ slabs were shorter and stronger than that of CuO/Cu_2O/

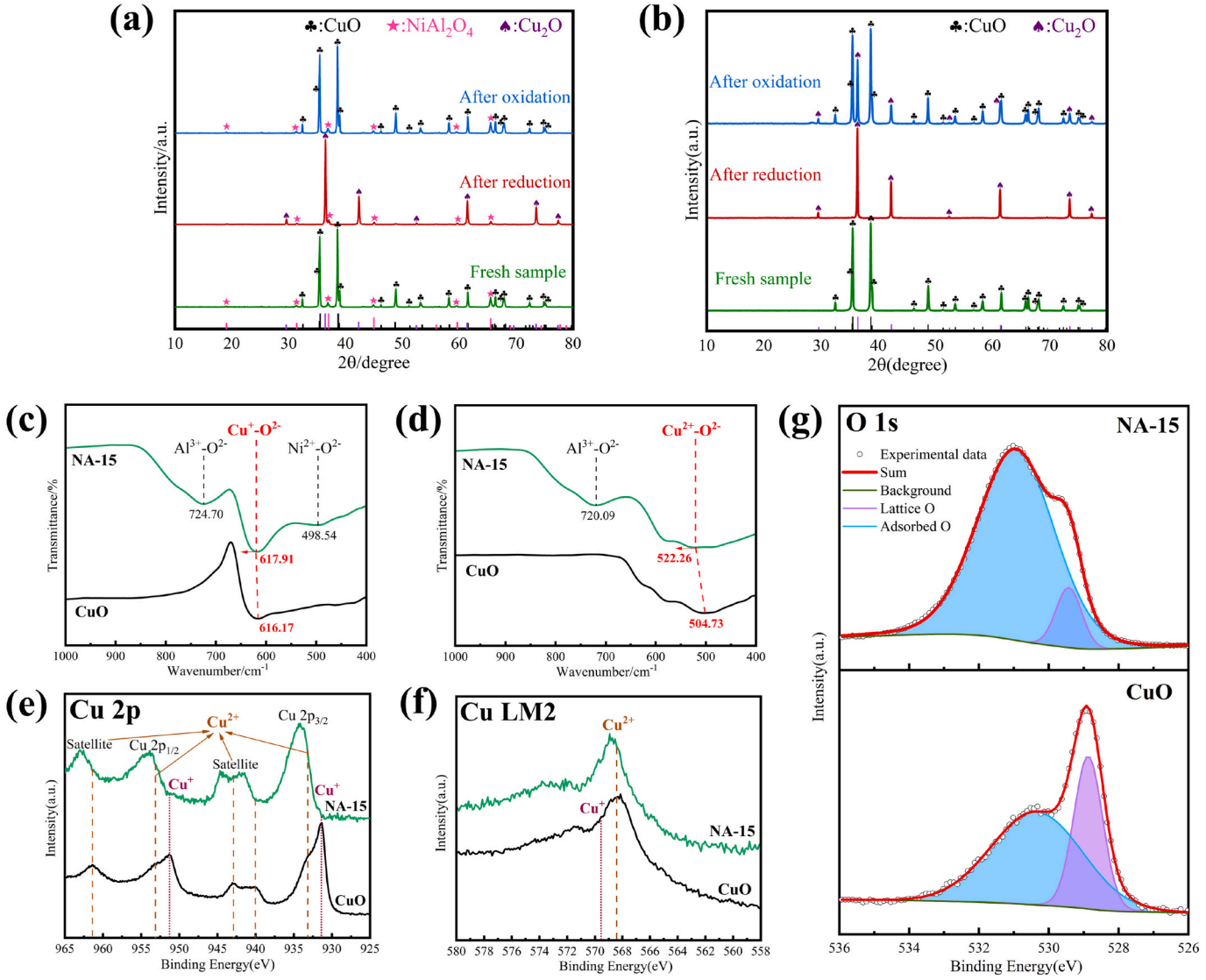

Fig. 7. Physicochemical properties characterization for NA-15 and CuO. XRD patterns of different stages (a) NA-15 and (b) CuO. Local enlargement FTIR spectra at the range of 1000–400 cm^{-1} (c) after reduction and (d) after 1st cycle. XPS spectra of (e) Cu 2p, (f) Cu LM2, (g) O1s after 1st cycle.

$NiAl_2O_4$ or CuO-CuO/Cu_2O-Cu_2O. The results expounded that it was more difficult to break bonds in this system, and there was a strong interaction between the $NiAl_2O_4$ and CuO/Cu_2O, which could inhibit the migration of CuO/Cu_2O at high temperature. In addition, according to the mass transfer through diffusion mechanism in solid state sintering theory, vacancy concentration in each part of the particle was different to some extent, and the concentration gradient promoted the diffusion of thermal defects such as vacancy on the surface or inside of the particle, thus accelerating the sintering. The copper vacancy formation energies of the interface models at different layers are presented in Fig. 9c and d. E(V_{Cu}) had the order of CuO-CuO < CuO-$NiAl_2O_4$ and Cu_2O-Cu_2O < Cu_2O-$NiAl_2O_4$, elucidating that the copper vacancies in CuO/Cu_2O after $NiAl_2O_4$ decoration were more difficult to form, thereby slowing down the mass transfer during sintering. Theoretically, enhancing the strong interfacial interaction between the inhibitor and the sintered material, and restraining the formation of copper vacancy can effectively improve the sintering resistance of the material.

Based on the experimental characterization and DFT calculation results, the redox modification mechanism of self-assembly CuO/Cu_2O with $NiAl_2O_4$ surface decoration was clarified, as shown in Fig. 10. When CuO/Cu_2O undergoes reversible redox transformation, the spinel structure $NiAl_2O_4$ inhibitor with excellent thermal stability maintains phase stability to avoid impurity damage reactivity. The inhibitor with smaller particle size can retain more CuO/Cu_2O reaction area. The inert inhibitor is distributed at the CuO/Cu_2O grain boundary, and the driving force of CuO/Cu_2O grain growth is offset by the Zener pinning force acting on the grain boundary by $NiAl_2O_4$, thus effectively inhibiting grain growth. Moreover, $NiAl_2O_4$ is uniformly dispersed on the surface of CuO/Cu_2O, acting as a physical barrier to spatially confine the metal oxides from sintering. Simultaneously, there is a strong interaction between metal oxides and inhibitor, increasing the formation energy of copper vacancy. Thus, the binding firmness of inhibitor and CuO/Cu_2O during the cycle is ensured, and the sintering of CuO/Cu_2O caused by surface bonding and mass transfer is inhibited. To conclude, CuO/Cu_2O modified by appropriate amount of $NiAl_2O_4$ have excellent redox reversibility and long cycle life.

4. Conclusions

In summary, we have successfully synthesized the self-assembled CuO surface decorated with 15 wt% $NiAl_2O_4$. The performance test results showed that the oxidation rate increased by 4.2 times, and the re-oxidation degree increased from 46 % to 99.9 %. The chemical energy density of storage and release reached −772.726 kJ/kg and 764.655 kJ/

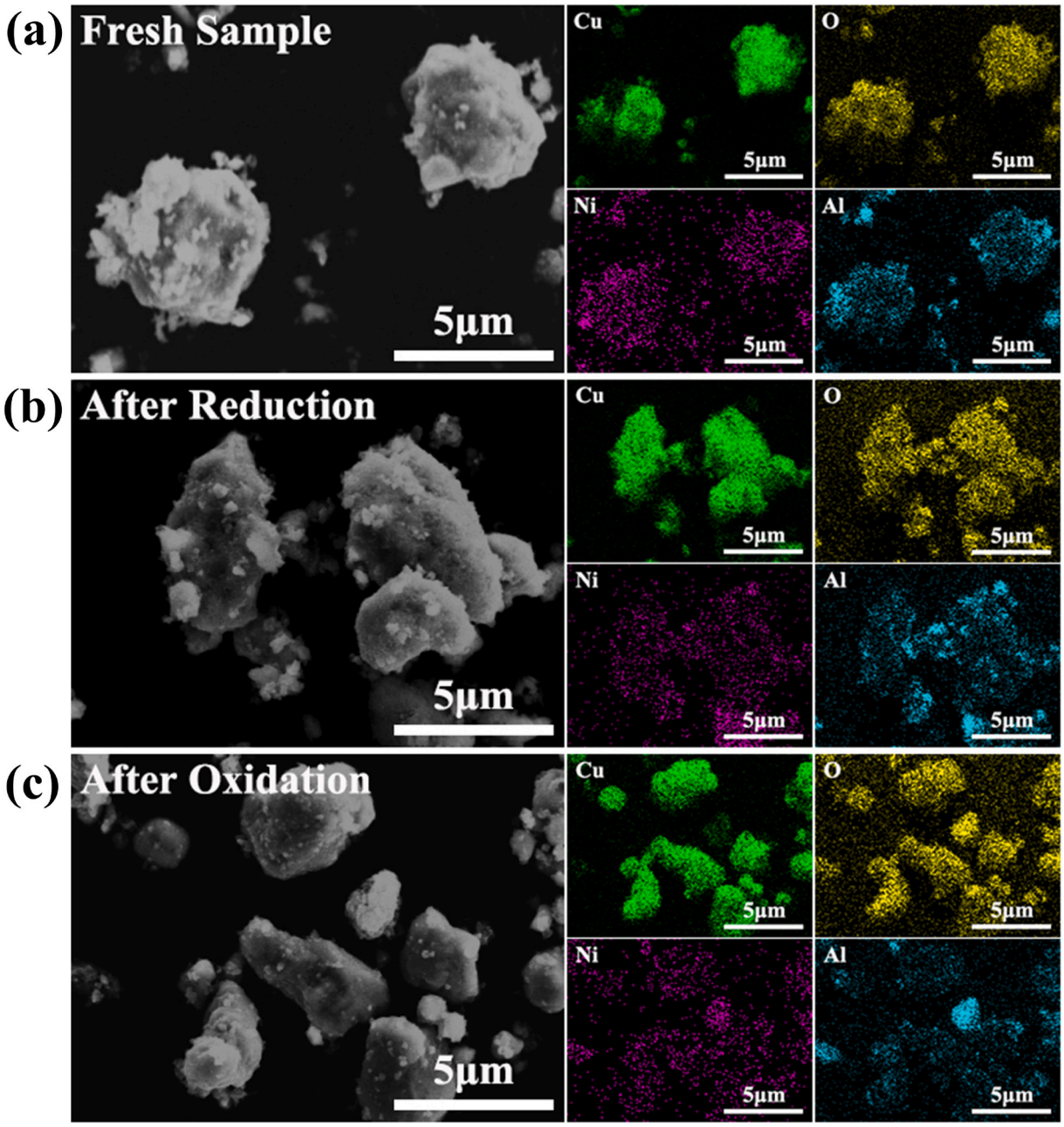

Fig. 8. SEM images and corresponding EDS elemental mappings of NA-15: (a) fresh sample, (b) after reduction and (c) after 1st cycle.

kg. Moreover, the oxidation degree kept 98 % after 1000 cycles. Material characterization demonstrated that the $NiAl_2O_4$ inhibitor as a physical barrier uniformly dispersed on the CuO/Cu_2O surface. And more oxygen vacancies in $NiAl_2O_4$ contributed to the bonding between CuO/Cu_2O and $NiAl_2O_4$ surface, greatly increasing the sintering temperature. DFT results further confirmed the strong interaction between CuO/Cu_2O and $NiAl_2O_4$, and the introduction of $NiAl_2O_4$ increased the formation energy of copper vacancy in the system, which effectively solved the problems of sintering. The integration of experimental and computational effort offers deep insights into the modification mechanism of anti-sintering and redox activity of CuO surface decorated with $NiAl_2O_4$. These results can provide ideas for the development of cost-effective and simpler synthesis methods, as well as the rational design of high-performance, long-life thermochemical energy storage materials with sintering resistance.

CRediT authorship contribution statement

Jiali Deng: Conceptualization, Methodology, Software, Investigation, Writing – original draft. **Changdong Gu:** Validation, Writing – review & editing. **Haoran Xu:** Visualization, Writing – review & editing. **Gang Xiao:** Resources, Supervision, Project administration, Funding acquisition.

Declaration of competing interest

The authors declare that they have no known competing financial interests or personal relationships that could have appeared to influence the work reported in this paper.

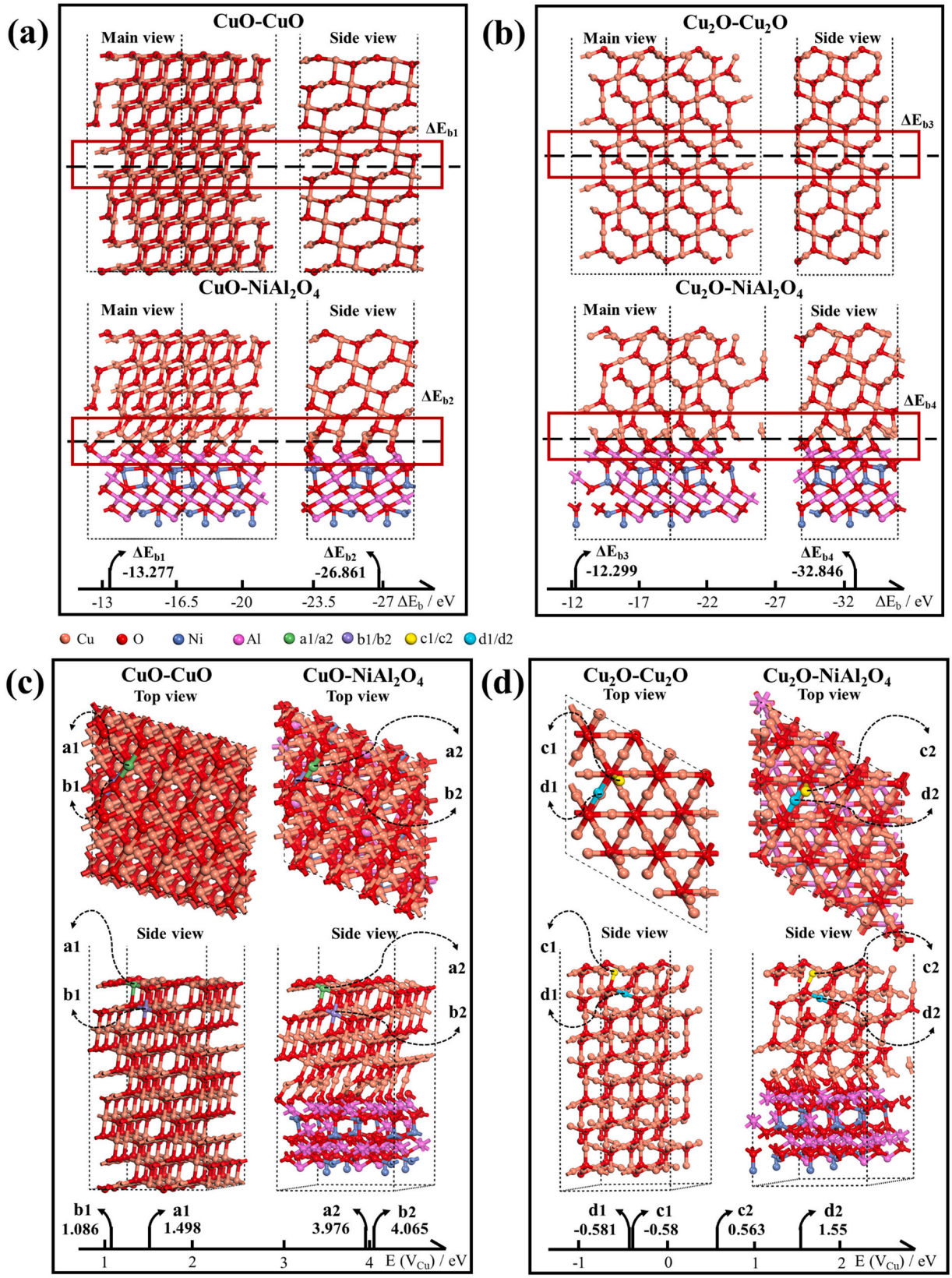

Fig. 9. DFT calculations. Interface binding energy ΔE_b of (a) CuO-CuO and CuO-$NiAl_2O_4$, (b) Cu_2O-Cu_2O and Cu_2O-$NiAl_2O_4$; Formation energies of copper vacancy E (V_{Cu}) at different sites of (c) CuO-CuO and CuO-$NiAl_2O_4$, (d) Cu_2O-Cu_2O and Cu_2O-$NiAl_2O_4$.

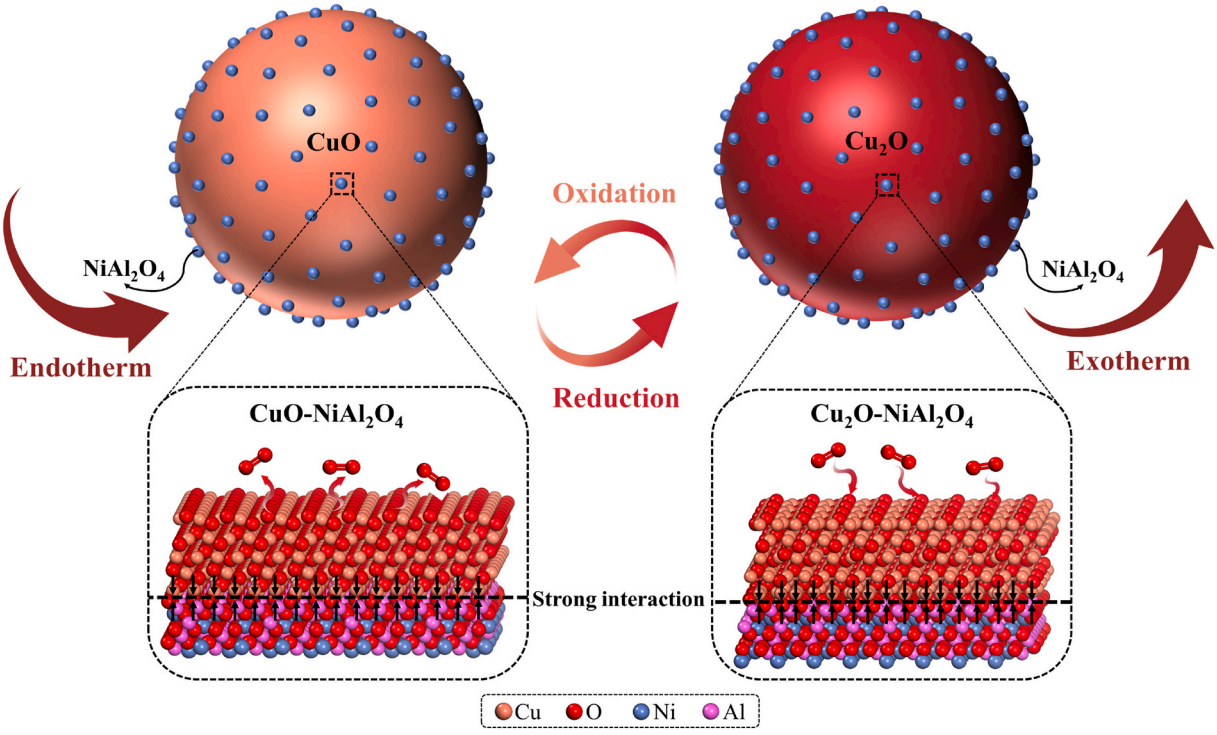

Fig. 10. Schematic of redox and anti-sintering modification mechanism of CuO/Cu_2O with $NiAl_2O_4$ surface decoration.

Data availability

Data will be made available on request.

Acknowledgments

This work was supported by the Zhejiang Science Foundation for Distinguished Young Scholars (LR20E060001); the National Natural Science Foundation of China (52176207); and the Fundamental Research Funds for the Central Universities (2022ZFJH004).

Appendix A. Supplementary data

Supplementary data to this article can be found online at https://doi.org/10.1016/j.est.2022.106370.

References

[1] L.A. Weinstein, J. Loomis, B. Bhatia, D.M. Bierman, E.N. Wang, G. Chen, Concentrating solar power, Chem. Rev. 115 (2015) 12797–12838, https://doi.org/10.1021/acs.chemrev.5b00397.
[2] A.J. Carrillo, J. González-Aguilar, M. Romero, J.M. Coronado, Solar energy on demand: a review on high temperature thermochemical heat storage systems and materials, Chem. Rev. 119 (2019) 4777–4816, https://doi.org/10.1021/acs.chemrev.8b00315.
[3] A. Solé, I. Martorell, L.F. Cabeza, State of the art on gas-solid thermochemical energy storage systems and reactors for building applications, Renew. Sust. Energ. Rev. 47 (2015) 386–398, https://doi.org/10.1016/j.rser.2015.03.077.
[4] C. Agrafiotis, M. Roeb, C. Sattler, Hybrid sensible/thermochemical solar energy storage concepts based on porous ceramic structures and redox pair oxides chemistry, Energy Procedia 69 (2015) 706–715, https://doi.org/10.1016/j.egypro.2015.03.081.
[5] A.J. Carrillo, D. Sastre, D.P. Serrano, P. Pizarro, J.M. Coronado, Revisiting the BaO2 /BaO redox cycle for solar thermochemical energy storage, Phys. Chem. Chem. Phys. 18 (2016) 8039–8048, https://doi.org/10.1039/C5CP07777J.
[6] T. Kousksou, P. Bruel, A. Jamil, T. El Rhafiki, Y. Zeraouli, Energy storage: applications and challenges, Sol. Energy Mater. Sol. Cells 120 (2014) 59–80, https://doi.org/10.1016/j.solmat.2013.08.015.
[7] E. Alonso, C. Pérez-Rábago, J. Licurgo, E. Fuentealba, C.A. Estrada, First experimental studies of solar redox reactions of copper oxides for thermochemical energy storage, Sol. Energy 115 (2015) 297–305, https://doi.org/10.1016/j.solener.2015.03.005.
[8] L. André, S. Abanades, G. Flamant, Screening of thermochemical systems based on solid-gas reversible reactions for high temperature solar thermal energy storage, Renew. Sust. Energ. Rev. 64 (2016) 703–715, https://doi.org/10.1016/j.rser.2016.06.043.
[9] S. Wu, C. Zhou, E. Doroodchi, R. Nellore, B. Moghtaderi, A review on high-temperature thermochemical energy storage based on metal oxides redox cycle, Energy Convers. Manag. 168 (2018) 421–453, https://doi.org/10.1016/j.enconman.2018.05.017.
[10] T. Block, M. Schmücker, Metal oxides for thermochemical energy storage: a comparison of several metal oxide systems, Sol. Energy 126 (2016) 195–207, https://doi.org/10.1016/j.solener.2015.12.032.
[11] J.S. Prasad, P. Muthukumar, F. Desai, D.N. Basu, M.M. Rahman, A critical review of high-temperature reversible thermochemical energy storage systems, Appl. Energy 254 (2019), 113733, https://doi.org/10.1016/j.apenergy.2019.113733.
[12] A. Bayon, R. Bader, M. Jafarian, L. Fedunik-Hofman, Y. Sun, J. Hinkley, S. Miller, W. Lipiński, Techno-economic assessment of solid–gas thermochemical energy storage systems for solar thermal power applications, Energy 149 (2018) 473–484, https://doi.org/10.1016/j.energy.2017.11.084.
[13] A.J. Schrader, A.P. Muroyama, P.G. Loutzenhiser, Solar electricity via an air Brayton cycle with an integrated two-step thermochemical cycle for heat storage based on Co3O4/CoO redox reactions: thermodynamic analysis, Sol. Energy 118 (2015) 485–495, https://doi.org/10.1016/j.solener.2015.05.045.
[14] C. Agrafiotis, S. Tescari, M. Roeb, M. Schmücker, C. Sattler, Exploitation of thermochemical cycles based on solid oxide redox systems for thermochemical storage of solar heat. Part 3: cobalt oxide monolithic porous structures as integrated thermochemical reactors/heat exchangers, Sol. Energy 114 (2015) 459–475, https://doi.org/10.1016/j.solener.2014.12.037.
[15] A.P. Muroyama, A.J. Schrader, P.G. Loutzenhiser, Solar electricity via an air Brayton cycle with an integrated two-step thermochemical cycle for heat storage based on Co3O4/CoO redox reactions II: kinetic analyses, Sol. Energy 122 (2015) 409–418, https://doi.org/10.1016/j.solener.2015.08.038.
[16] D. Müller, C. Knoll, W. Artner, M. Harasek, C. Gierl-Mayer, J.M. Welch, A. Werner, P. Weinberger, Combining in-situ X-ray diffraction with thermogravimetry and differential scanning calorimetry-an investigation of Co3O4, MnO2 and PbO2 for thermochemical energy storage, Sol. Energy 153 (2017) 11–24, https://doi.org/10.1016/j.solener.2017.05.037.
[17] L. André, S. Abanades, L. Cassayre, High-temperature thermochemical energy storage based on redox reactions using co-fe and mn-fe mixed metal oxides, J. Solid State Chem. 253 (2017) 6–14, https://doi.org/10.1016/j.jssc.2017.05.015.
[18] L. André, S. Abanades, L. Cassayre, Experimental investigation of co-cu, mn-co, and mn-cu redox materials applied to solar thermochemical energy storage, ACS Appl. Energy Mater. 1 (2018) 3385–3395, https://doi.org/10.1021/acsaem.8b00554.
[19] A.J. Carrillo, D.P. Serrano, P. Pizarro, J.M. Coronado, Improving the thermochemical energy storage performance of the Mn2O3/Mn3O4 redox couple by the incorporation of iron, ChemSusChem 8 (2015) 1947–1954, https://doi.org/10.1002/cssc.201500148.
[20] C. Agrafiotis, T. Block, M. Senholdt, S. Tescari, M. Roeb, C. Sattler, Exploitation of thermochemical cycles based on solid oxide redox systems for thermochemical

storage of solar heat. Part 6: testing of mn-based combined oxides and porous structures, Sol. Energy 149 (2017) 227–244, https://doi.org/10.1016/j.solener.2017.03.083.
[21] M. Wokon, T. Block, S. Nicolai, M. Linder, M. Schmücker, Thermodynamic and kinetic investigation of a technical grade manganese-iron binary oxide for thermochemical energy storage, Sol. Energy 153 (2017) 471–485, https://doi.org/10.1016/j.solener.2017.05.045.
[22] D. Xiang, C. Gu, H. Xu, G. Xiao, Self-assembled structure evolution of mn-fe oxides for high temperature thermochemical energy storage, Small 17 (2021), 2101524, https://doi.org/10.1002/smll.202101524.
[23] M. Deutsch, F. Horvath, C. Knoll, D. Lager, C. Gierl-Mayer, P. Weinberger, F. Winter, High-temperature energy storage: kinetic investigations of the CuO/Cu2O reaction cycle, Energy Fuel 31 (2017) 2324–2334, https://doi.org/10.1021/acs.energyfuels.6b02343.
[24] C. Agrafiotis, M. Roeb, C. Sattler, Exploitation of thermochemical cycles based on solid oxide redox systems for thermochemical storage of solar heat. Part 4: screening of oxides for use in cascaded thermochemical storage concepts, Sol. Energy 139 (2016) 695–710, https://doi.org/10.1016/j.solener.2016.04.034.
[25] S. Setoodeh Jahromy, F. Birkelbach, C. Jordan, C. Huber, M. Harasek, A. Werner, F. Winter, Impact of partial pressure, conversion, and temperature on the oxidation reaction kinetics of Cu2O to CuO in thermochemical energy storage, Energies 12 (2019) 508, https://doi.org/10.3390/en12030508.
[26] M. Gigantino, S. Sas Brunser, A. Steinfeld, High-temperature thermochemical heat storage via the CuO/Cu2O redox cycle: from material synthesis to packed-bed reactor engineering and cyclic operation, Energy Fuel 34 (2020) 16772–16782, https://doi.org/10.1021/acs.energyfuels.0c02572.
[27] Q. Imtiaz, M. Broda, C.R. Müller, Structure-property relationship of co-precipitated cu-rich, Al2O3-or MgAl2O4-stabilized oxygen carriers for chemical looping with oxygen uncoupling (CLOU), Appl. Energy 119 (2014) 557–565, https://doi.org/10.1016/j.apenergy.2014.01.007.
[28] D. Xiang, C. Gu, H. Xu, J. Deng, P. Zhu, G. Xiao, Al-modified CuO/Cu2O for high-temperature thermochemical energy storage: from reaction performance to modification mechanism, ACS Appl. Mater. Interfaces 13 (2021) 57274–57284, https://doi.org/10.1021/acsami.1c17592.
[29] G. Kresse, D. Joubert, From ultrasoft pseudopotentials to the projector augmented-wave method, Phys. Rev. B 59 (1999) 1758, https://doi.org/10.1103/PhysRevB.59.1758.
[30] G. Kresse, J. Furthmüller, Efficient iterative schemes for ab initio total-energy calculations using a plane-wave basis set, Phys. Rev. B 54 (1996) 11169, https://doi.org/10.1103/PhysRevB.54.11169.
[31] J.P. Perdew, K. Burke, M. Ernzerhof, Generalized gradient approximation made simple, Phys. Rev. Lett. 77 (1996) 3865, https://doi.org/10.1103/PhysRevLett.77.3865.
[32] S.L. Dudarev, G.A. Botton, S.Y. Savrasov, C.J. Humphreys, A.P. Sutton, Electron-energy-loss spectra and the structural stability of nickel oxide: an LSDA+ U study, Phys. Rev. B 57 (1998) 1505, https://doi.org/10.1103/PhysRevB.57.1505.
[33] M. Nolan, S.D. Elliott, The p-type conduction mechanism in Cu2O: a first principles study, Phys. Chem. Chem. Phys. 8 (2006) 5350–5358, https://doi.org/10.1039/B611969G.
[34] B. Wang, J. Nisar, R. Ahuja, Molecular simulation for gas adsorption at NiO (100) surface, ACS Appl. Mater. Interfaces 4 (2012) 5691–5697, https://doi.org/10.1021/am3016894.
[35] B.Z. Sun, X.L. Xu, W.K. Chen, L.H. Dong, Theoretical insights into the reaction mechanisms of NO oxidation catalyzed by Cu2O (1 1 1), Appl. Surf. Sci. 316 (2014) 416–423, https://doi.org/10.1016/j.apsusc.2014.06.178.
[36] J. Hu, D. Li, J.G. Lu, R. Wu, Effects on electronic properties of molecule adsorption on CuO surfaces and nanowires, J. Phys. Chem. C 114 (2010) 17120–17126, https://doi.org/10.1021/jp1039089.
[37] S. Karmakar, D. Behera, Non-overlapping small polaron tunneling conduction coupled dielectric relaxation in weak ferromagnetic NiAl2O4, J. Phys. Condens. Matter 31 (2019), 245701, https://doi.org/10.1088/1361-648X/ab03f0.
[38] M.A. Khan, M. Ullah, T. Iqbal, H. Mahmood, A.A. Khan, M. Shafique, A. Majid, A. Ahmed, N.A. Khan, Surfactant assisted synthesis of cuprous oxide (Cu2O) nanoparticles via solvothermal process, Nanosci. Nanotechnol. Res. 3 (2015) 16–22, https://doi.org/10.12691/nnr-3-1-3.
[39] S.K. Shinde, D.P. Dubal, G.S. Ghodake, P. Gomez-Romero, S. Kim, V.J. Fulari, Influence of mn incorporation on the supercapacitive properties of hybrid CuO/Cu(OH)2 electrodes, RSC Adv. 5 (2015) 30478–30484, https://doi.org/10.1039/C5RA01093D.
[40] K. Wang, X. Dong, C. Zhao, X. Qian, Y. Xu, Facile synthesis of Cu2O/CuO/RGO nanocomposite and its superior cyclability in supercapacitor, Electrochim. Acta 152 (2015) 433–442, https://doi.org/10.1016/j.electacta.2014.11.171.
[41] Q. Zhang, L. Huang, S. Kang, C. Yin, Z. Ma, L. Cui, Y. Wang, CuO/Cu2O nanowire arrays grafted by reduced graphene oxide: synthesis, characterization, and application in photocatalytic reduction of CO2, RSC Adv. 7 (2017) 43642–43647, https://doi.org/10.1039/C7RA07310K.
[42] X. Tang, B. He, J. Li, G. Qin, One-step preparation of Cu/BC catalyzed the upgrading of heavy oil assisted by microwave, J. Pet. Sci. Eng. 208 (2022), 109683, https://doi.org/10.1016/j.petrol.2021.109683.
[43] X. Yang, W. Liu, G. Pan, Y. Sun, Modulation of oxygen in NiO: cu films toward a physical insight of NiO: Cu/c-si heterojunction solar cells, J. Mater. Sci. 53 (2018) 11684–11693, https://doi.org/10.1007/s10853-018-2430-1.
[44] I.A. Khan, A. Badshah, M.A. Nadeem, N. Haider, M.A. Nadeem, A copper based metal-organic framework as single source for the synthesis of electrode materials for high-performance supercapacitors and glucose sensing applications, Int. J. Hydrog. Energy 39 (2014) 19609–19620, https://doi.org/10.1016/j.ijhydene.2014.09.106.
[45] X. Fang, R. Zhang, Y. Wang, M. Yang, Y. Guo, M. Wang, J. Zhang, J. Xu, X. Xu, X. Wang, Plasma assisted preparation of highly active NiAl2O4 catalysts for propane steam reforming, Int. J. Hydrog. Energy 46 (2021) 24931–24941, https://doi.org/10.1016/j.ijhydene.2021.05.050.
[46] W. Wang, Z. Qu, L. Song, Q. Fu, An investigation of Zr/Ce ratio influencing the catalytic performance of CuO/Ce1-xZrxO2 catalyst for CO2 hydrogenation to CH3OH, J. Energy Chem. 47 (2020) 18–28, https://doi.org/10.1016/j.jechem.2019.11.021.